

Solid-State Lithium/Selenium–Sulfur Chemistry Enabled via a Robust Solid-Electrolyte Interphase

Gui-Liang Xu, Hui Sun, Chao Luo, Luis Estevez, Minghao Zhuang, Han Gao, Rachid Amine, Hao Wang, Xiaoyi Zhang, Cheng-Jun Sun, Yuzi Liu, Yang Ren, Steve M. Heald, Chunsheng Wang, Zonghai Chen,* and Khalil Amine*

Lithium/selenium-sulfur batteries have recently received considerable attention due to their relatively high specific capacities and high electronic conductivity. Different from the traditional encapsulation strategy for suppressing the shuttle effect, an alternative approach to directly bypass polysulfide/polyselenide formation via rational solid-electrolyte interphase (SEI) design is demonstrated. It is found that the robust SEI layer that in situ forms during charge/discharge via interplay between rational cathode design and optimal electrolytes could enable solid-state (de)lithiation chemistry for selenium-sulfur cathodes. Hence, Se-doped $S_{22.2}Se$ /Ketjenblack cathodes can attain a high reversible capacity with minimal shuttle effects during long-term and high rate cycling. Moreover, the underlying solid-state (de)lithiation mechanism, as evidenced by in situ 7Li NMR and in operando synchrotron X-ray probes, further extends the optimal sulfur confinement pore size to large mesopores and even macropores that have been long considered as inferior sulfur or selenium host materials, which play a crucial role in developing high volumetric energy density batteries. It is expected that the findings in this study will ignite more efforts to tailor the compositional/structure characteristics of the SEI layers and the related ionic transport across the interface by electrode structure, electrolyte solvent, and electrolyte additive screening.

1. Introduction

The urgent demand on the development of power sources for electric vehicles has created many opportunities for new energy storage systems.^[1] In the past decades, lithium/sulfur (Li/S) battery has received considerable attention because of its high energy density ($\approx 2600 \text{ Wh kg}^{-1}$) and the natural abundance of elemental sulfur.^[2] However, the poor electronic conductivity of sulfur and its discharge products (Li_2S/Li_2S_2) presents a critical barrier for high-performance sulfur cathodes with high reversible capacity, long cycle life, and high rate capability.^[3,4] A relatively high amount of conductive carbon is usually required to ensure efficient electron transport within the sulfur electrodes to enable high utilization of the insulating sulfur. However, carbon is usually electrochemically inactive and thus decreases the overall capacity of the sulfur electrode. Recently, lithium/selenium (Li/Se) battery has attracted research interest

Dr. G.-L. Xu, M. Zhuang, H. Gao, H. Wang, Z. H. Chen, K. Amine
Chemical Sciences and Engineering Division
Argonne National Laboratory
Lemont, IL 60439, USA
E-mail: zonghai.chen@anl.gov; amine@anl.gov

Dr. H. Sun
State Key Laboratory of Heavy Oil Processing
Institute of New Energy
China University of Petroleum-Beijing
Beijing 102249, China

Dr. C. Luo, Prof. C. Wang
Department of Chemical and Biomolecular Engineering
University of Maryland
College Park, MD 20742, USA

Dr. L. Estevez
Energy and Environment Directorate
Pacific Northwest National Laboratory
Richland, WA 99354, USA

R. Amine
Materials Science Division
Argonne National Laboratory
Lemont, IL 60439, USA

Dr. X. Zhang, C.-J. Sun, Y. Ren, S. M. Heald
X-Ray Science Division
Argonne National Laboratory
Lemont, IL 60439, USA

Dr. Y. Liu
Center for Nanoscale Materials
Argonne National Laboratory
Lemont, IL 60439, USA

Dr. K. Amine
Materials Science and Engineering
Stanford University
Stanford, CA 94305, USA

 The ORCID identification number(s) for the author(s) of this article can be found under <https://doi.org/10.1002/aenm.201802235>.

DOI: 10.1002/aenm.201802235

due to its comparable volumetric capacity to Li/S battery (3268 mAh cm^{-3} vs 3467 mAh cm^{-3} for sulfur) and the high electronic conductivity of Se (25 orders of magnitude higher than sulfur).^[5] These properties could enable an ultrahigh loading of Se in the electrodes without having to consider the electronic conductivity issue. Therefore, exploration of Se-S cathodes that have both high electronic conductivity and high specific capacity is a promising strategy to enable high-performance and high-loading Li/S batteries.^[6,7]

The electrochemical performance of Li/S and Li/Se-S batteries highly depends on the electrolytes used in the system. To the best of our knowledge, carbonate-based and ether-based electrolytes are two of the mostly deployed electrolytes so far. It is widely accepted that Li/S and Li/Se-S undergo a solid-state lithiation process in the carbonate electrolytes without any formation of soluble polysulfides/polyselenides.^[8–10] However, the nucleophilic attack of soluble polysulfides and Li_2S toward carbonate solvents such as ethylene carbonate and ethyl methyl carbonate raises a big concern on directly using sulfur particles in the carbonate electrolytes without protection.^[11,12] Guo and co-workers have reported a smart strategy by using small sulfur allotropes S_{2-4} , which were confined in a microporous carbon matrix (MPC) with an extreme small pore size of $\approx 0.5 \text{ nm}$.^[13] Although the resulted $\text{S}_{2-4}/\text{MPC}$ composite showed admirable electrochemical properties, the sulfur loading was significantly limited to only 40 wt% due to the low pore volume of MPC.

On the other hand, Li/S and Li/Se-S batteries undergo a two-step solid–liquid–solid (de)lithiation process in the conventional ether-based electrolytes, in which sulfur (selenium) was reduced to Li_2S (Li_2Se) via highly soluble polysulfides (polyselenides) intermediates.^[14,15] Soon after Nazar and co-workers^[14] reported that ordered mesoporous carbon significantly improves the electrochemical performance of the sulfur cathode, numerous efforts have been devoted to find optimal conductive host materials that confine sulfur and polysulfides within the cathode side through either physical adsorption^[16–19] or chemical interactions such as polar–polar interaction^[20,21] and metal–sulfur bonding.^[22,23] However, as long as the generation of soluble polysulfides/polyselenides intermediates, performance degradation due to the loss of active materials and the shuttle effect is just a matter of time. Moreover, by using in situ Se K-edge X-ray absorption near-edge spectroscopy (XANES), we have recently found that space-confined Se-S cathodes would still undergo continuously capacity fade and severe shuttle effect even though Se-S was well encapsulated into the porous carbon matrix due to a distinct binding sequence between polysulfides/polyselenides and carbon host.^[24]

Compared to the extensive efforts on the cathode side, less attention has been paid to manipulate the interfacial chemistry resulted from the interplay between rational cathode design and optimal electrolytes, which could significantly affect the electrochemistry of Se-S cathodes. Herein, we have demonstrated an alternative approach to the traditional sulfur-encapsulation strategy via a rational solid-electrolyte interphase (SEI) design to directly bypass the polysulfides/polyselenides formation. As evidenced by in situ ^7Li NMR spectroscopy and in operando synchrotron X-ray probes during electrochemical cycling, we found that the SEI layer that in situ formed on the

surface of Se-S cathodes has switched their lithiation chemistry from conventional two-step solid–liquid–solid reaction to one-step solid-state (de)lithiation process. Therefore, the formation of polysulfides/polyselenides was dramatically inhibited as further confirmed by high-precision leakage current measurement. An amorphous Se-doped $\text{S}_{22.2}\text{Se}/\text{Ketjenblack}$ cathode with extraordinary electrochemical performance was hence developed. More importantly, our work also enables the use of high pore volume (6 cc g^{-1}) large porous carbon ($\approx 40 \text{ nm}$) as a promising host material for high-loading Se-S cathodes (up to 85 wt%) to increase the volumetric energy density of batteries. This study indicates that manipulating the SEI chemistry could open up new avenues for the development of high-performance rechargeable battery systems.

2. Results and Discussion

Understanding the physical properties of Se-S compounds is critical to develop high-performance Se-S cathodes. Thus, a series of bulk Se-S compounds were prepared by heating mixtures of S and Se in designated weight ratios at $600 \text{ }^\circ\text{C}$ for 3 h through a vapor-condensation method. **Figure 1a** shows the Raman spectra of S, Se, and Se-S compounds. As shown, with increasing S content, the characteristic peaks of S gradually increase while the intensities of the Se peaks decrease accordingly. **Figure 1b** depicts the high-energy X-ray diffraction (HEXRD) patterns of the various Se-S compounds, in which we can see that most of these compounds are crystalline. It is unexpected to find that bulk S_3Se_5 , S_1Se_1 , and S_5Se_4 are in an amorphous state. **Figure 1c** further shows the pair distribution function analysis of S powder, Se-S compounds, and Se powder. We can see the chemical environment significantly changed with different S concentrations. These data suggest that the as-prepared Se-S compounds are a series of new materials rather than a simple physical mixture of S and Se. Their theoretical capacities are compared in **Figure S1** (Supporting Information), which shows that capacity decreases with decreasing S content. By contrast, the electronic conductivity should increase with increasing Se content. Therefore, optimal Se-S compounds could be promising cathode materials with high specific capacity, high electronic conductivity, and low cost. Take S_5Se_2 as an example. It has a theoretical capacity of 1389 mAh g^{-1} , while the weight ratio between element Se and S is close to 1/1, which should be more conductive than bare S. Therefore, S_5Se_2 was chosen as a model material to investigate the electrochemistry of Se-S cathodes.

Similar to the previously reported space-confined S- and Se-based cathodes, we prepared an $\text{S}_5\text{Se}_2/\text{Ketjenblack}$ (hereafter $\text{S}_5\text{Se}_2/\text{KB}$) composite through the melt-impregnation method.^[16,17] The HEXRD patterns of the $\text{S}_5\text{Se}_2/\text{KB}$ composite (**Figure 1d**) show that no diffraction peaks belong to crystalline sulfur, selenium, or S_5Se_2 can be observed, indicating that S_5Se_2 nanoparticles are well encapsulated into the pores of the Ketjenblack and exist in an amorphous state. The content of S_5Se_2 in the composite was determined to be about 50 wt% by thermogravimetric analysis (TGA) of the $\text{S}_5\text{Se}_2/\text{KB}$ composite under an argon atmosphere (**Figure 1e**). The scanning electron microscopy (SEM) image (**Figure 1f**) and the corresponding

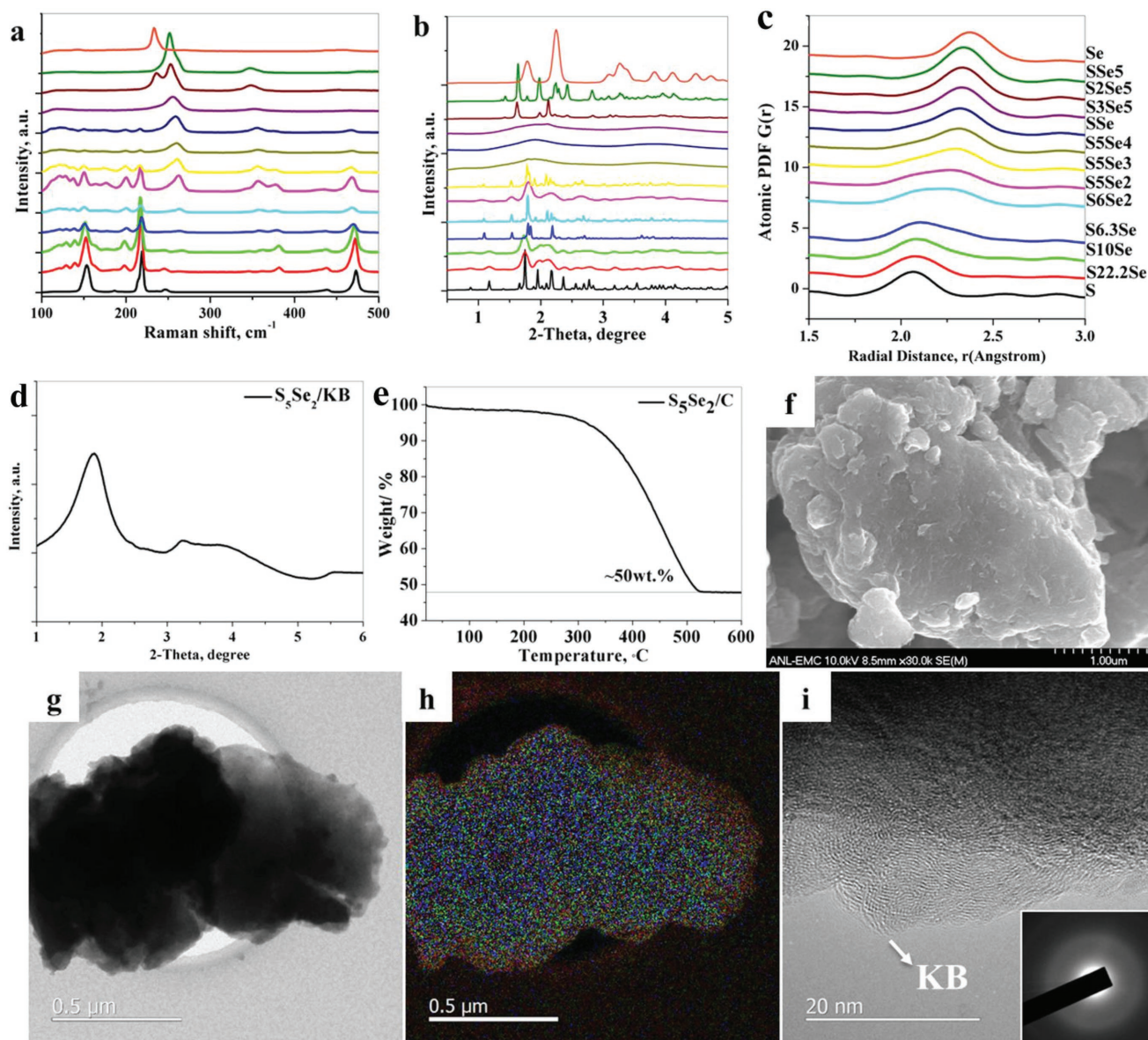


Figure 1. a) Raman, b) HEXRD, and c) pair distribution function analysis of bulk Se-S compounds. Color coding in panel (c) also applies to panels (a) and (b). d) HEXRD, e) TGA under argon atmosphere, f) SEM image, g) TEM image, h) corresponding elemental map, and i) high-resolution TEM image of space-confined S_5Se_2 /KB composite. The line color in panels (a)–(c) corresponds to an increase of S content in Se-S compounds. Inset of panel (i) is the SAED pattern. The red represents carbon; the blue represents sulfur; and the green represents selenium in panel (h).

elemental map (Figure S2, Supporting Information) show that the S_5Se_2 nanoparticles are well assembled with Ketjenblack to form microsize secondary particles. The transmission electron microscopy (TEM) image (Figure 1g) and the corresponding elemental mapping (Figure 1h) further showed that carbon, sulfur, and selenium are uniformly distributed throughout the S_5Se_2 /KB composite. The high-resolution TEM image (Figure 1i) and the selected area electron diffraction (SAED) pattern (inset) confirmed that S_5Se_2 was in an amorphous state. These structural features are similar to the previously reported space-confined Se-S cathodes,^[25–30] and this correspondence can help us to identify common issues during the electrochemical reaction.

The electrochemical performance of the S_5Se_2 /KB cathode was evaluated by assembling electrodes into coin cells with lithium as the reference and counter electrode. **Figure 2a–c** shows the voltage–capacity curve for the first discharge of the S_5Se_2 /KB cathode in the carbonate-, 1,2-dimethoxyethane (DME)-, and HFE-based electrolyte at C/20 ($1C = 1389 \text{ mA g}^{-1}$), respectively. DME-based electrolyte is the conventional ether-based electrolyte for Li/S battery (i.e., 1 M lithium bis(trifluoromethanesulfonyl)imide (LiTFSI)/1,3-dioxolane (DOL)+DME (1/1, v/v) with $LiNO_3$ additive), while HFE-based electrolyte has the same formula except DME is replaced by HFE. DME is a linear ether, while HFE is a hydrofluoro-ether (see their molecule structures in Table S1, Supporting

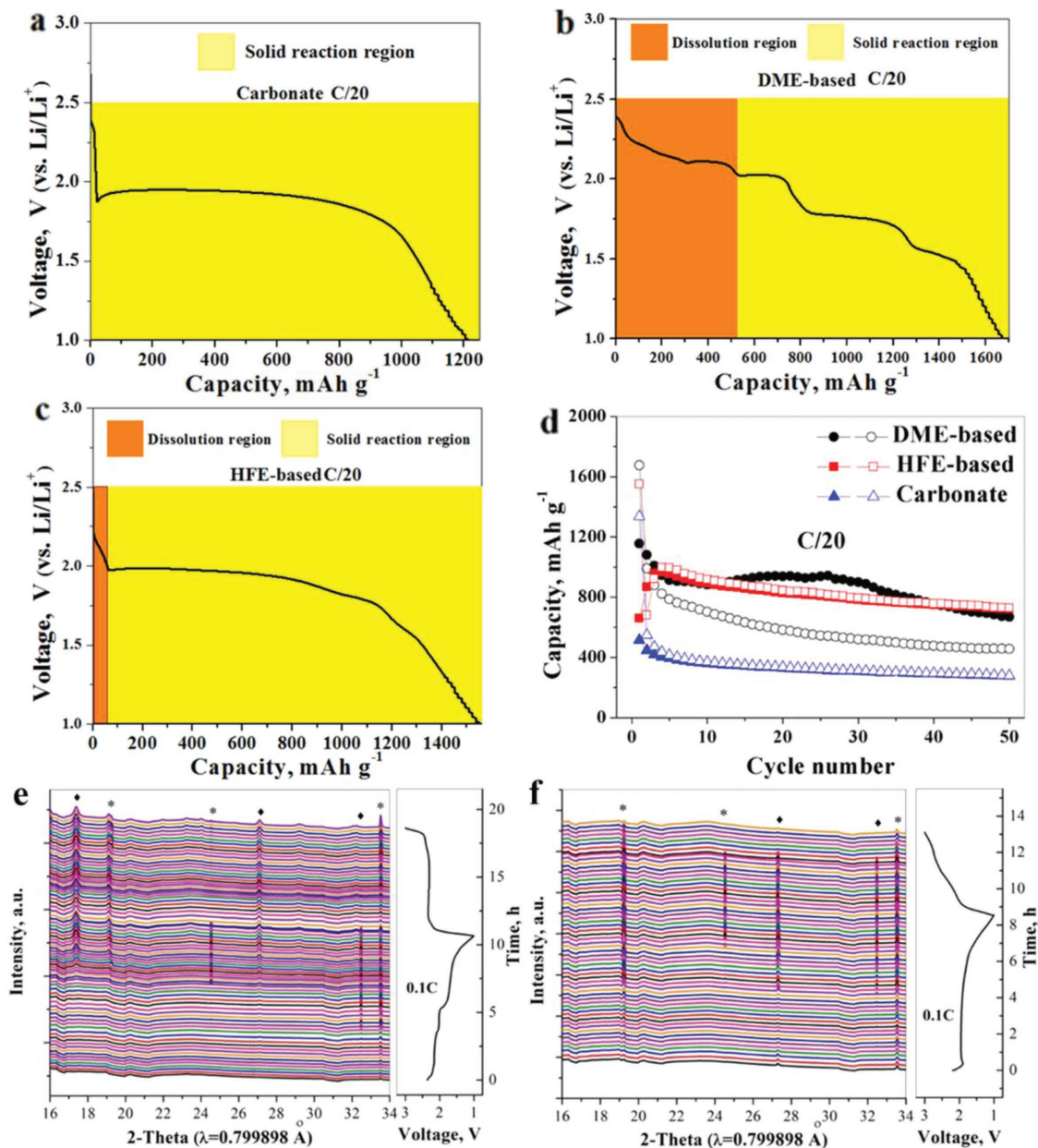


Figure 2. The first discharge curve of S_5Se_2 /KB cathode in a) carbonate-based, b) DME-based, and c) HFE-based electrolyte at C/20. d) Cycling performance of S_5Se_2 /KB cathode in the three electrolytes. Open symbols indicate discharge; solid symbols mean charge in panel (d). In operando HEXRD patterns collected during the first cycle of space-confined S_5Se_2 /KB cathode at C/10 in e) DME-based and f) HFE-based electrolyte. The diamond represents Li_2S , and the star represents Li_2Se in panels (e) and (f).

Information). Figure 2a clearly shows a single discharge plateau in the carbonate-based electrolyte, corresponding to the direct electrochemical transformation of S_5Se_2 to Li_2S / Li_2Se without the formation of soluble polysulfides/polyselenides, which has been proved to be a solid-state lithiation/delithiation reaction by advanced spectroscopy analyses.^[8,31,32] For the DME-based electrolyte (Figure 2b), there are multiple discharge voltage plateaus, which can be assigned to the well-known two-step solid-liquid-solid reactions of Li with S_5Se_2 , respectively.^[33] The upper voltage plateau was generally attributed to the dissolution region, while the lower voltage plateau was related to the

formation of solid Li_2S and Li_2Se .^[34] In addition, a small plateau was observed at ≈ 1.6 V, which was related to the reduction of $LiNO_3$ additive.^[35] In the HFE-based electrolyte (Figure 2c), the single long discharge plateau indicates a solid-solid lithiation-delithiation process, while the short sloping region may correspond to the formation of trace polysulfides/polyselenides in the initial discharge stage.

Figure 2d shows the cycle performance of the S_5Se_2 /KB cathode in three different electrolytes at C/20. The S_5Se_2 /KB cathode can only deliver a capacity of around 300 mAh g^{-1} in the carbonate electrolyte, which can be ascribed to the widely

reported poor compatibility of Li/S battery with carbonate electrolytes.^[32] Figure S3a (Supporting Information) shows the electrochemical performance of S/KB cathode in the carbonate electrolyte, which quickly faded in few cycles. In fact, in order to enable the use of Li/S battery in the carbonate electrolytes, a physical barrier to isolate sulfur species and carbonate solvent is necessary. While in the case of Li/Se battery, a lot of reports have shown that it is much more compatible with carbonate electrolytes than Li/S battery. Li et al. have reported that amorphous S-rich $S_{1-x}Se_x/C$ cathode could demonstrate much better electrochemical performance than S/C cathode without Se.^[7] Figure S3b (Supporting Information) shows the electrochemical performance of Se/KB composite in the carbonate electrolyte, which can deliver a stable capacity of around 400 mAh g⁻¹ with single discharge plateau of ≈1.8 V. That is the reason why the S_5Se_2/KB material can still deliver 300 mAh g⁻¹ in the carbonate electrolyte, in which the capacity is mainly from the contribution of Se redox reaction. In the DME-based electrolyte, the cathode showed continuous capacity degradation over 50 cycles, together with severe shuttle effect. This result is similar to the previously reported Se-based cathodes and was attributed to the aggravation formation of highly soluble long-chain polyselenides during cycling.^[24] As a comparison, after an activation process in the initial three cycles, the S_5Se_2/KB cathode in the HFE-based electrolyte attained a much higher reversible capacity of over 700 mAh g⁻¹ and displayed minimal shuttle effect within 50 cycles. This may result from its solid-solid (de)lithiation mechanism, which can bypass the formation of soluble polysulfides/polyselenides during electrochemical cycling.

To clearly unravel the reaction mechanism of the S_5Se_2/KB cathode in DME- and HFE-based electrolytes, in operando synchrotron HEXRD studies were carried out to monitor their structural evolution during the charge/discharge process. Coin cell with a 3 mm hole on the top and bottom cases and sealed with Kapton film was used for HEXRD experiment (Figure S4a, Supporting Information). Figure 2e shows the in operando HEXRD patterns of the S_5Se_2/KB cathode in the DME-based electrolyte together with its first discharge/charge curve at C/10. In the figure, multiple discharge voltage plateaus can be clearly seen, corresponding to the commonly reported two-step reactions from S_5Se_2 to Li_2S_n/Li_2Se_n ($n \geq 4$) and then Li_2S/Li_2Se .^[33] It can be clearly seen that the diffraction peaks of Li_2S and Li_2Se can be well indexed during the discharge process. During charge, a long charge plateau was observed, which should be related to the oxidation of Li_2S and Li_2Se to long-chain polysulfides/polyselenides. However, at the end of the first charge process, the diffraction peaks of Li_2S and Li_2Se could still be seen, indicating a large amount of solid products (Li_2S and Li_2Se) remained in the electrode.^[36] It can be clearly seen that the intensities for the diffraction peaks of Li_2Se (33.5°) was increased during charge (Figure S5, Supporting Information), indicating that it is formed by chemical reaction between long-chain Li_2Se_n and the Li anode rather than electrochemical reduction of Se or long-chain polyselenides (impossible during charge). Therefore, the above parasitic reactions of long-chain polyselenides are the main cause for the poor electrochemical performance of the S_5Se_2/KB cathode in the DME-based electrolyte, a finding that coincides with our previous study.^[24]

The electrochemistry and structural evolution of the S_5Se_2/KB cathode in the HFE-based electrolyte is shown in Figure 2f, which also involved the formation of crystalline Li_2S and Li_2Se during discharge. Nevertheless, only a small amount of residual crystalline Li_2Se is evident at the end of the charge. This was attributed to the sluggish electrochemical oxidation kinetics of Li_2Se in the HFE-based electrolyte (due to solid state), thus leading to the capacity activation process in the initial three cycles. Figure S6a,b (Supporting Information) shows the first discharge/charge curves of S/KB and Se/KB cathodes at C/20 in the HFE-based electrolytes, respectively. As can be seen, they both present a single discharge plateau. Therefore, we speculate that the interplay between space-confined Se-S cathodes and HFE-based electrolyte could enable a solid-solid (de)lithiation process for Se-S/KB cathodes.

To confirm this hypothesis, we carried out in situ ⁷Li NMR spectroscopy, as it is very sensitive to the solid and liquid Li⁺ species inside the test cells. The solid components generally result in broader signals while the solution components usually present narrow line widths due to the presence of anisotropic interactions. The electrochemistry of the Li/S system in the DME-based electrolyte has been explored by Grey and co-workers,^[37] who found that the S is reduced to soluble polysulfide species concurrently with the formation of a solid component (Li_2S) at the beginning of the first plateau, and the second plateau is defined by the reduction of the residual soluble species to solid product. In this work, a pouch cell (Figure S4b, Supporting Information) was used for in situ ⁷Li NMR measurement to explore the nature of the possible intermediates and products formed during the lithiation/delithiation of the S_5Se_2/KB cathode in the HFE-based electrolyte.

Figure 3a shows the typical ⁷Li NMR spectra of the pristine S_5Se_2/KB cathode before charge/discharge, which shows two sharp signals including one at higher frequency and one at lower frequency. The NMR spectra can be well fitted by two resolvable peaks with a high overlap of 91.3% by using the software suite included in Topspin 3.1. This is similar to the results reported by Grey and co-workers,^[37] and the peaks may be assigned to the soluble Li⁺ species in the cell. It is hard to distinguish the contributions of either electrolyte or other battery components, such as $LiNO_3$ additive, to the peaks. Nonetheless, the noticeable changes in intensity for these two sharp signals during charge/discharge are generally ascribed to the formation/decomposition of soluble polysulfides or polyselenides.^[38] When the cell was discharged to 1.0 V, as shown in Figure 3b, in addition to two sharp signals from the soluble Li⁺ species, a broad resonance signal is apparent, which is related to the formation of a Li⁺-containing solid species such as Li_2S and Li_2Se .^[38] When the cell was charged back to 3.0 V (Figure 3c), the intensity of these two sharp peaks changed very little while the broad signal decreased but did not completely disappear. This finding indicates that some of the Li⁺-containing solid species were oxidized, and some remained in the electrode at the end of the charge, a finding that is in good agreement with the in operando HEXRD result.

Figure 3d shows the 2D contour plot of the in operando NMR spectra of the S_5Se_2/KB cathode in the HFE-based electrolyte along with the first discharge/charge curve at C/30. The color represents the intensity of the NMR signals, with red

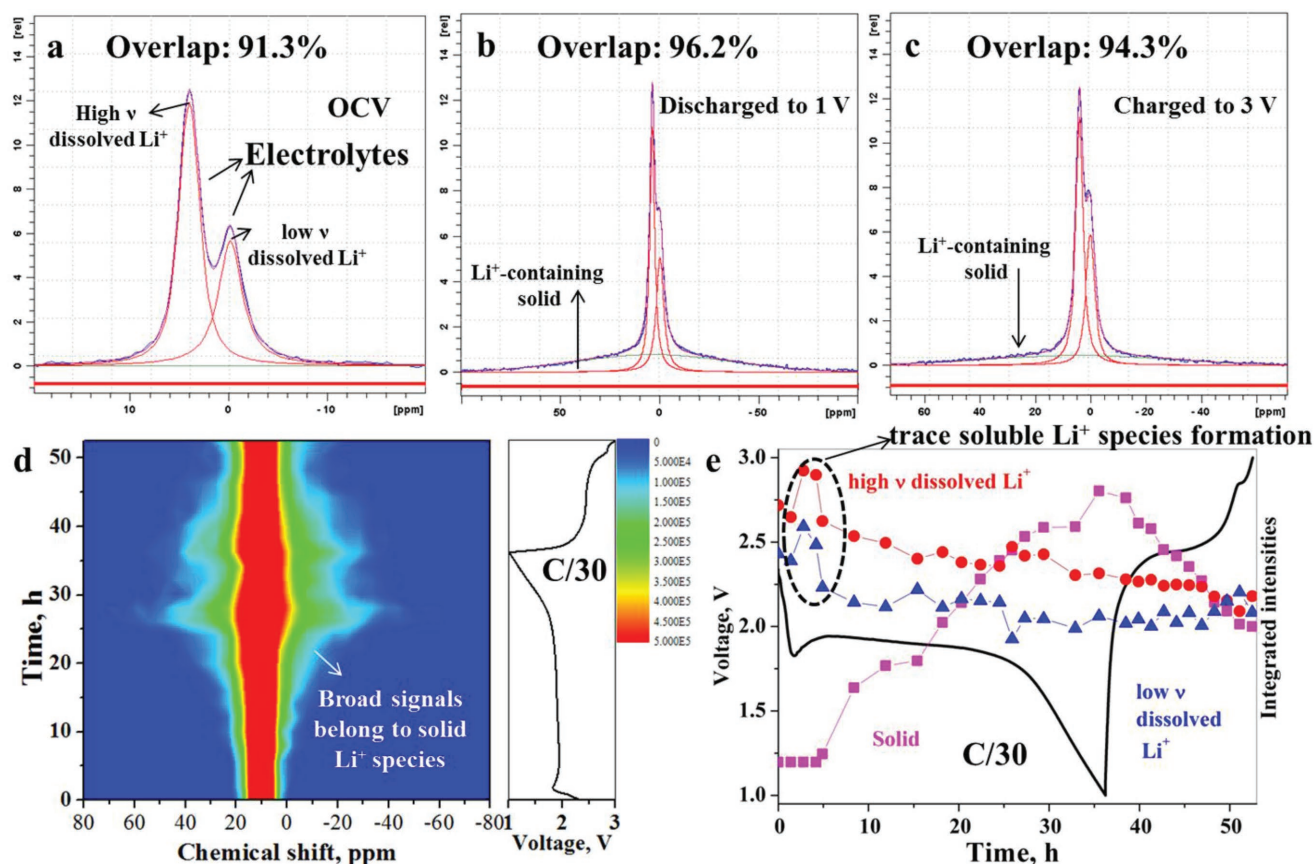


Figure 3. In operando ^7Li NMR studies of the $\text{S}_5\text{Se}_2/\text{KB}$ cathode in the HFE-based electrolyte: fit curves to the NMR line shape at a) open circuit voltage, b) discharged to 1.0 V, and c) charged back to 3.0 V. d) 2D contour plot of NMR signal versus charge/discharge curve at C/30; e) integrated areas of Li^+ species as a function of charge/discharge process.

being high intensity and blue being low intensity. As shown, as the discharge proceeded, different from the results in the DME-based electrolyte reported by Grey and co-workers^[37] and Wang et al.,^[38] the intensities of two sharp signals (represented by the red color) changed little while the signal of the broad resonance gradually increased, indicating more Li^+ -containing solid formation. During charge, the signals for the Li^+ -containing solid gradually decreased. To quantify the change of the soluble and solid Li^+ species, in situ NMR data were fit by fixing the widths of the sharp resonances but allowing the line width of the broad resonance to float. Good fits were obtained throughout (see Figure S7, Supporting Information).^[37] The integrated areas along with the charge/discharge process are compared in Figure 3e. As shown, the integrated areas of the soluble Li^+ species at both high and low frequency slightly increase at the very beginning of the discharge and then keep relatively stable for the remaining charge/discharge process, which means that a small amount of polysulfides/polyselenides formation occurred during the early discharge stage in the HFE-based electrolyte, a finding that is consistent with the prediction from the voltage profiles. Moreover, the integrated area of the Li^+ -containing solid changed little at the very beginning of the discharge. However, its intensity was significantly increased after the consumption of the trace polysulfides/polyselenides and reached

a maximum at the end of discharge. During charge, the integrated area of solid Li^+ species gradually decreased, while the soluble Li^+ species remained relatively stable. Hence, in operando ^7Li NMR study revealed very little soluble polysulfides/polyselenides formation in the HFE-based electrolyte during the whole charge/discharge process, and most of the S_5Se_2 was converted directly to Li_2S and Li_2Se , indicating a solid–solid lithiation–delithiation process.

To further confirm this conclusion, we carried out in operando Se K-edge X-ray absorption near edge spectroscopy (XANES) on the fourth cycle of the $\text{S}_5\text{Se}_2/\text{KB}$ cathode in the HFE-based electrolyte to bypass the activation process in the initial three cycles. Figure 4a shows a 2D contour plot for the in operando Se K-edge XANES data at C/10. As shown, the absorption intensity of Se (12 658 eV) gradually decreased during the discharge and was completely recovered at the end of charge. Representative Se XANES spectra during the discharge/charge process are shown in Figure S8 (Supporting Information), in which no energy shift for Se from 12 658 to 12 665 eV is evident. This is consistent with our previous result for carbonate-based electrolyte^[8] and different from that for DME-based electrolyte.^[15] Therefore, we concluded that Se-S/KB cathodes undergo a solid-state lithiation/delithiation process in the HFE-based electrolyte. Note that although hydrofluoroether electrolyte has been previously reported for S cathodes by others,^[39,40]

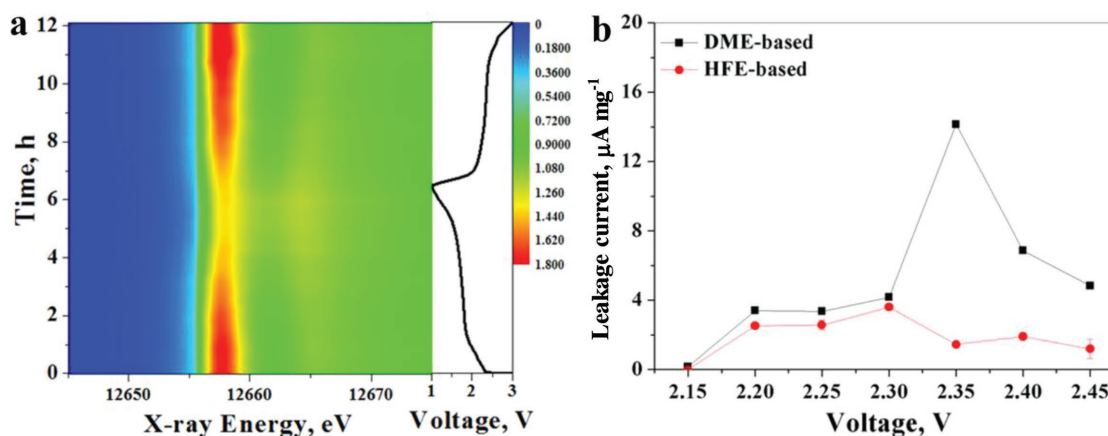


Figure 4. a) In operando Se K-edge XANES on the fourth cycle of S_5Se_2 /KB cathode at C/10 in HFE-based electrolyte, and b) leakage current of S_5Se_2 /KB cathode in DME- and HFE-based electrolytes.

their main focus is the suppressed polysulfides dissolution and enhanced solvation capability. What we are looking in this work is the unexpected solid–solid lithiation chemistry resulting from the interplay between rational cathode design and optimal electrolyte. This process is critical to improve the shuttle effect and cycle life, as it directly bypasses the formation of soluble polysulfides/polyselenides.

Figure 4b further compares the parasitic reactions of the Se-S/KB cathode in the DME- and HFE-based electrolytes as measured by our home-built high-precision leakage current measurement system.^[41–44] The cells were discharged/charged for two cycles and then charged to a different potential and held for 20 h to obtain the equilibrium current. The measured leakage current (i) is proportional to the reaction rate of the parasitic reactions between the potentially formed polysulfides/polyselenides and Li anode during charge. Hence, the static leakage current can be used as a quantitative indicator for polysulfide/polyselenide shuttle. As shown in Figure 4b, the largest leakage current in the HFE-based electrolyte is only one-fourth that in the DME-based electrolyte, indicating a significantly improved shuttle effect.

By only changing the solvent from DME to HFE and keeping the other components the same, we observed the switch of reaction pathway from solid–liquid–solid to solid–solid. In another word, the solid–solid lithiation process should come from the contribution of HFE, and $LiNO_3$ did not play a critical role in enabling the solid–solid lithiation process. We have further prepared an electrolyte without $LiNO_3$ (1 M LiTFSI/DOL+HFE (1/1, v/v)). As shown in Figure S9 (Supporting Information), without $LiNO_3$, Se/Ketjenblack composite still presented single discharge voltage plateau and no clear shuttle effect can be observed during cycling, indicating a possibility of using an electrolyte without $LiNO_3$. This solvent-induced reaction pathway change may depend on the charge/discharge rate, which may bypass the formation of some intermediates, such as soluble long-chain polysulfides/polyselenides, owing to electrochemical polarization. Therefore, the Li/ S_5Se_2 cell was charge/discharged in the HFE-based electrolyte at a very low rate of C/100 ($1C = 1389 \text{ mA g}^{-1}$). As shown in Figure S10 (Supporting Information), the voltage–capacity curve still

presents a single discharge plateau rather than the multiple discharge plateaus displayed with the DME-based electrolyte. This finding indicates that the solid–solid (de)lithiation process of Se-S cathodes in the HFE-based electrolyte is not kinetic-controlled. The solid-state lithiation chemistry would not come from the suppressed polysulfides dissolution in the HFE-based electrolytes either. For example, Suo et al. have reported a solvent-in-salt electrolyte for Li/S batteries, in which polysulfide dissolution was inhibited as confirmed by the polysulfides dissolution test and the ultraviolet–visible result.^[45] However, it still presented two lithiation plateaus in the voltage profile, corresponding to a two-step solid–liquid–solid lithiation reaction and formation of soluble polysulfides. We have further conducted density functional theory (DFT) calculation to determine the solvation energies of polysulfides in the DOL, DME, and HFE, which had been used to predict the solubility of species in different solvent.^[46] The ground-state molecular structures of polysulfides were fully optimized at the B3LYP/6-31G(d) level, and their energies are shown in Figure S11 (Supporting Information). The solvation energies of polysulfides in different solvents were investigated by using the solvation model based on density (SMD). As shown in Table S1 (Supporting Information), the solvation energies of polysulfides (e.g., Li_2S_4) in the HFE are all close to those value in the DME and DOL, which should not cause significant lithiation chemistry change as observed.

To understand the mechanism behind the solid–solid lithiation chemistry, we have further conducted X-ray photoelectron spectroscopy (XPS) characterization on the cycled electrodes to unravel the compositional/structure characteristics of the interfacial layers and the related ionic transport across the interface in Li/Se-S batteries. Figure 5a–d shows the XPS characterization result of discharged $S_{22.2}Se$ /KB cathode in different electrolytes. Compared to the one in DME-based electrolyte, there is an obvious formation of SEI layer on the surface of $S_{22.2}Se$ /KB cathode material when discharged in the HFE-based electrolyte. This can be confirmed by the evolution of C1s peaks for $-CF_3$ ($\approx 294 \text{ eV}$) and $-C=C-$ ($\approx 284 \text{ eV}$) bond due to the decomposition of HFE solvent and also enhanced S2p peaks of sulfate and sulfite ($166\text{--}172 \text{ eV}$) due to the increased reduction

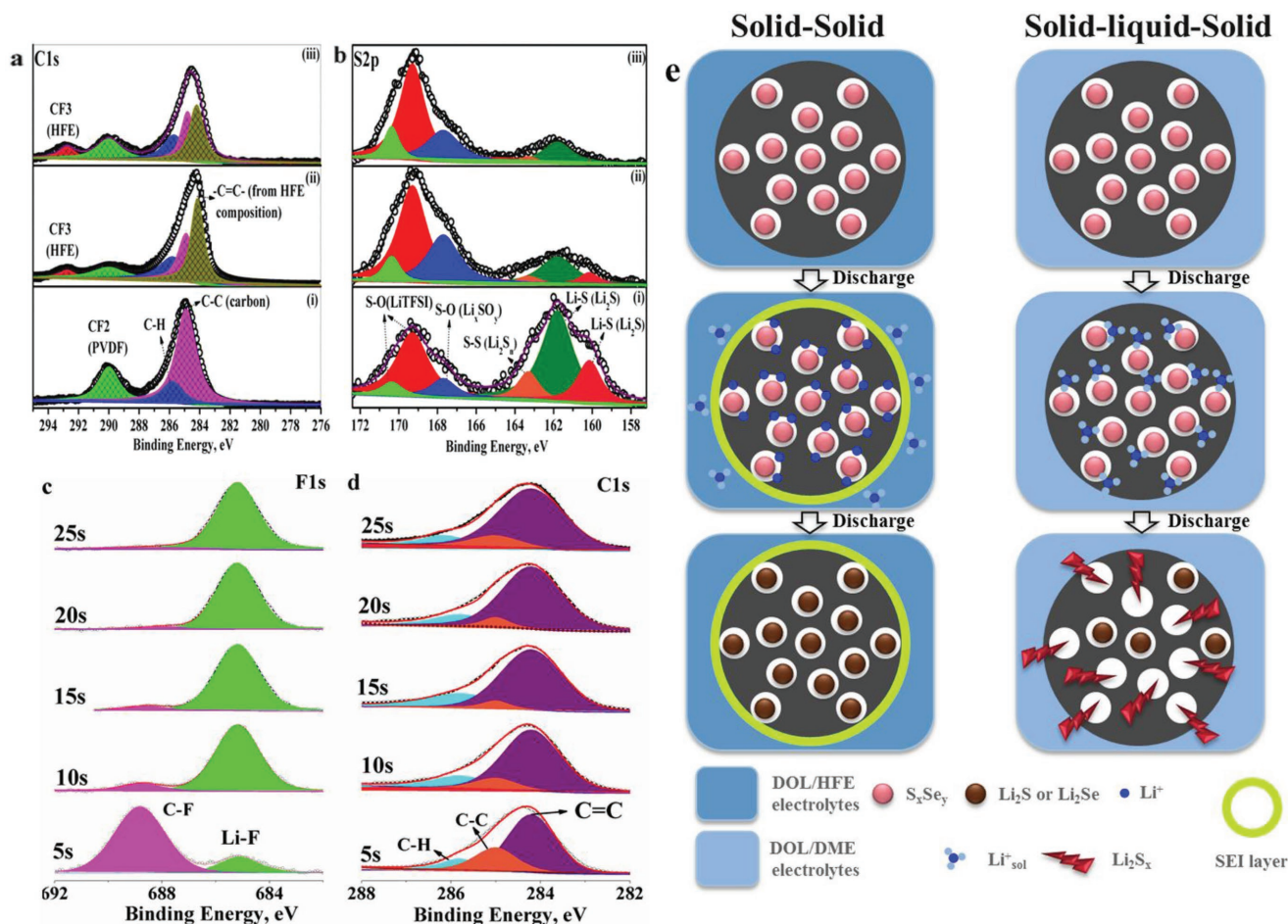


Figure 5. a) C1s and b) S2p X-ray photoelectron spectroscopy (XPS) spectra of first discharged $S_{22.2}Se/KB$ cathode in (i) DME-based, (ii) HFE-based electrolyte, (iii) first discharged S/KB cathode in HFE-based electrolytes; XPS spectra of c) F1s and d) C1s of first discharged $S_{22.2}Se/KB$ cathode in HFE-based electrolytes after different etching time; e) schematic illustration for different lithiation mechanism of Se-S cathodes in HFE-based and DME-based electrolytes.

of LiTFSI salt. XPS sputtering experiment further confirmed the formed SEI layer is robust. The SEM images (Figure S12, Supporting Information) of discharged electrodes in different electrolytes also showed that without the formation of SEI layer, lots of plate-like structures formed, indicating the dissolution of polysulfides/polyselenides from the carbon host. Similar plate-like discharge products formation has also been observed in the case of Li/S battery that undergoes severe shuttle effect using DOL/DME-based electrolytes.^[40,47] While no obvious structure changes can be observed in the HFE-based electrolytes, confirming bypassed formation of polysulfides/polyselenides via the help of SEI layer. Figure 5e shows the schematic illustration for different lithiation mechanism in different electrode/electrolyte systems. The origin of different lithiation mechanism in two different electrolytes for the same cathode structure should come from the in situ formed SEI layer, which can act as a physical barrier between electrode and electrolytes. In the HFE-based electrolyte, the formed robust SEI layer can desolvate Li^+ and prevent the attack of solvent molecules toward Se-S, and thus lead to the solid–solid lithiation process, while in the DME-based electrolytes, there is no such SEI formation and the solvated Li^+ can easily penetrate into the Se-S active material,

and thus lead to the formation of polysulfides/polyselenides and the solid–liquid–solid lithiation process.

According to the report by Liu and co-workers,^[48] SEI also formed outside the sulfur cathode in DME-based electrolyte. However, the charge/discharge curves also displayed two voltage plateaus in the reduction reaction, implying solid–liquid–solid lithiation process. We believe that it is the composition and distribution of SEI layer that play a significant role on tailoring the reaction pathway, which highly depend on the electrolytes and cathode structure. For example, $LiNO_3$ could decompose to form a passivation film consisting of LiN_xO_y on the surface of S cathode to suppress the shuttle effect but did not change the reaction pathway.^[24,49] In the result reported by Liu and co-workers,^[48] the main SEI composition are Li_2CO_3 and $ROCO_2Li$, which cannot invoke a solid–solid lithiation process either. In our result, the main SEI component came from the decomposition of HFE and LiTFSI salt, which both consist of $-CF_3$ in their molecular structures, leading to the formation of concentrated LiF and Li_xSO_y in the resulted SEI layer when the discharge cutoff voltage reached 1.0 V. As can be seen in Figure S13 (Supporting Information), without the formation of such SEI layer, S_5Se_2/KB cathode would still undergo two

discharge plateaus in the second cycle in the HFE-based electrolytes when it is cycled between 1.5 and 3.0 V. In this voltage region, it will form different SEI layer (mainly from the decomposition of LiNO_3 additive) from that in the voltage region of 1.0–3.0 V. Moreover, the distribution of the SEI layer will also affect the electrochemical behavior. Noted that the sulfur/carbon spheres composite reported by Liu and co-workers is crystalline,^[48] indicating part of sulfur may be deposited outside the carbon spheres. The electrochemical reduction of solvent and salt would prefer to take place on high conductivity area (carbon matrix in this case). Therefore, the sulfur particles outside the carbon spheres would not form such protective SEI layer, which will lead to the observed two-step solid–liquid–solid reaction. In our case, $\text{S}_5\text{Se}_2/\text{KB}$ material is amorphous, indicating that all the S_5Se_2 were encapsulated into the pores of KB. Hence, the SEI can deposit on the KB surface and thus prevent the contact between S_5Se_2 and the electrolytes and further solid–solid lithiation process.

The above results suggest that the dissolution of polysulfides/polyselenides can be inhibited by tailoring the (de)lithiation chemistry of space-confined Se-S cathodes. Since Se has a higher electronic conductivity but lower gravimetric capacity (675 mAh g^{-1}) than S, by rational design for the atomic ratio between S and Se, one can develop an optimal Se-S material with similar theoretical gravimetric capacity and improved electronic conductivity compared to S. In this work, an amorphous Se-doped $\text{S}_{22.2}\text{Se}/\text{KB}$ (50 wt%) cathode was further developed by adjusting the raw weight ratio between S and Se. The HEXRD pattern for the $\text{S}_{22.2}\text{Se}/\text{KB}$ composite in Figure S14 (Supporting Information) indicates that it is an amorphous structure. The composite shows similar morphology with the $\text{S}_5\text{Se}_2/\text{KB}$ composite for the SEM image in Figure S15a,b (Supporting Information), which indicates micro-sized secondary particles. The SEM elemental map (Figure S15c–f, Supporting Information) further confirmed that C, Se, and S are uniformly distributed in the composite without any aggregation. Figure 6a shows the charge/discharge curves of the $\text{S}_{22.2}\text{Se}/\text{KB}$ cathode in the initial three cycles at C/20 in the HFE-based electrolyte. The single long discharge voltage plateaus confirm a solid–solid (de)lithiation process. The initial discharge capacity was $1824.5 \text{ mAh g}^{-1}$, slightly exceeding the theoretical capacity of S. The excess capacity is due to the decomposition of LiNO_3 additive to form a surface protective layer on the Li anode to further prevent the shuttle effect.^[18] The initial charge capacity was $1307.9 \text{ mAh g}^{-1}$, leading to a high S utilization of around 80%. The voltage polarization decreased from the second cycle, owing to an activation process of solid–solid lithiation. Figure 6b shows the corresponding

cycle performance and coulombic efficiency upon charge/discharge at C/20. A high reversible capacity of $>1000 \text{ mAh g}^{-1}$ was maintained within 50 cycles, indicating good cycle stability. Moreover, the coulombic efficiency after the first cycle was very close to 100%, suggesting a significantly improved shuttle effect. Figure 6c further compares the rate capabilities of $\text{S}_{22.2}\text{Se}/\text{KB}$ and S/KB cathodes by continuously varying the current density. The curves clearly show that the $\text{S}_{22.2}\text{Se}/\text{KB}$ demonstrates much higher reversible capacity than Se-free S/KB at different current densities. This difference is likely owing to the higher electronic conductivity of Se than S, which can improve the poor electronic conductivity and the sluggish kinetics, especially during solid–solid (de)lithiation of Se-S cathodes. The average reversible capacity of the $\text{S}_{22.2}\text{Se}/\text{KB}$ cathode at C/20 was $1321.9 \text{ mAh g}^{-1}$, decreasing to $1179.2 \text{ mAh g}^{-1}$ at C/10, $1102.1 \text{ mAh g}^{-1}$ at C/5, $1006.2 \text{ mAh g}^{-1}$ at C/2.5, 911.3 mAh g^{-1} at 1C, 835.6 mAh g^{-1} at 2C, and 755.7 mAh g^{-1} at 4C. At an extreme high rate of 5C, which is equal to 8.4 A g^{-1} , a high reversible capacity of 707.5 mAh g^{-1} can still be maintained, indicating superior rate performance. Figure 6d further compares the cycling performance of $\text{S}_{22.2}\text{Se}/\text{KB}$ and S/KB cathode

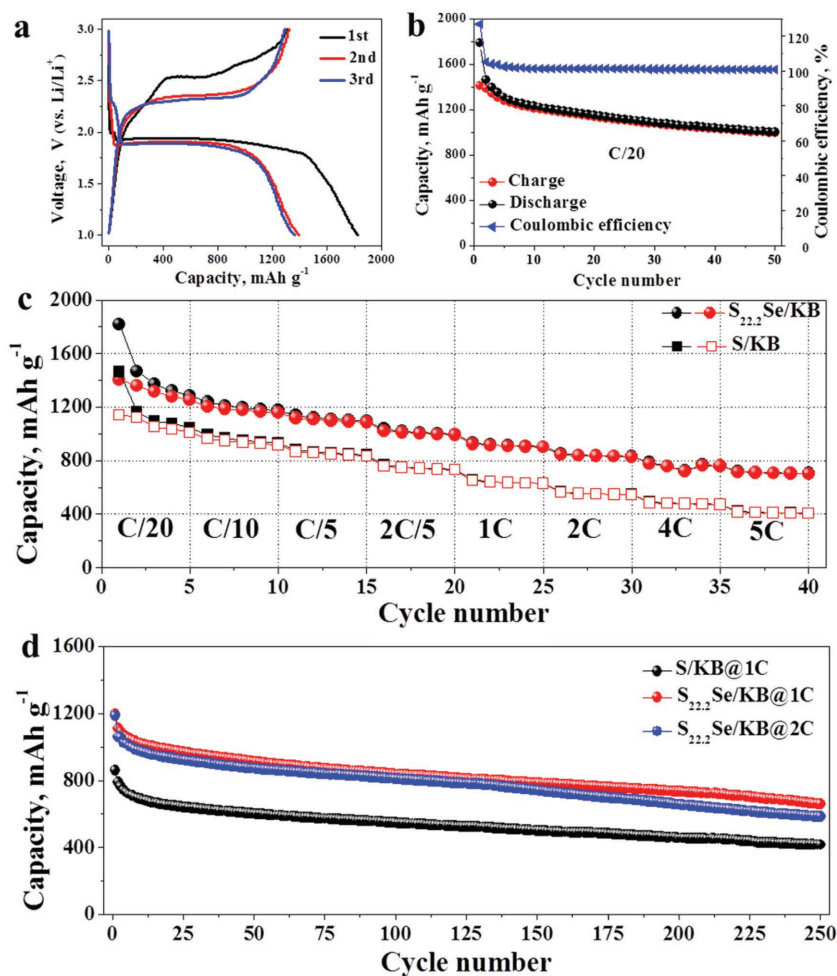


Figure 6. a) Charge/discharge curves and b) cycling performance of $\text{S}_{22.2}\text{Se}/\text{KB}$ cathode at C/20 in HFE-based electrolytes; c) rate performance and d) cycling performance at high rates of $\text{S}_{22.2}\text{Se}/\text{KB}$ cathode and S/KB cathode in HFE-based electrolyte.

at high rates. Both cathodes were cycled at C/20 for three cycles, and then the $S_{22.2}Se/KB$ cathode was cycled at 1C and 2C, and the S/KB cathode at 1C. After 250 cycles of charge/discharge at 1C and 2C, the $S_{22.2}Se/KB$ cathode still delivered a reversible capacity of 660 and 583 mAh g^{-1} , respectively, demonstrating excellent long-term cycle stability. By comparison, the S/KB cathode only maintained 417 mAh g^{-1} after 250 cycles at 1C. Despite the cycle stability difference, they both show coulombic efficiency close to 100% after the second cycle (Figure S16, Supporting Information), indicating a diminished shuttle effect in the HFE-based electrolyte. Therefore, by manipulating the SEI chemistry via the interplay between rational cathode design and optimal electrolyte, the dissolution of polysulfides/polyselenides, and the sluggish electrochemical reaction kinetics of S cathodes can be remarkably improved.

To attain higher energy densities, higher Se-S loading is needed in the composites and also in the electrodes. The loading in the electrodes could be further optimized through a laminate fabrication process^[50] and smart electrode structure design,^[51] while immobilizing polysulfides/polyselenides within the host materials should be at the core of high S loading system when using DME-based electrolytes. Considering the volume change from S ($\rho = 2.03 \text{ g cm}^{-3}$) to Li_2S ($\rho = 1.66 \text{ g cm}^{-3}$), we calculated the maximum S loading with respect to the pore volume of porous carbon. As shown in Figure S17a (Supporting Information), the required pore volume increased with increasing S loading. For example, for 70 wt% S loading, a pore volume of

at least 2.02 cc g^{-1} is required to constrain all the S in the pores and simultaneously accommodate the volume change during charge/discharge. However, this value is dramatically increased to as high as 4.91 cc g^{-1} for 85 wt% S loading. Such a high pore volume is rarely reported in microporous carbon (<2 nm) and small mesoporous carbon (2–10 nm). Figure S17b (Supporting Information) summarizes the pore size, pore volume, and the corresponding sulfur loading for various porous carbons in Li/S batteries from previously reported papers (see Table S2, Supporting Information). As shown, most of microporous carbons have a pore volume of $<1.0 \text{ cc g}^{-1}$, and their S loading is generally below 50%. The pore volumes of small mesoporous carbons (2–10 nm) are in the range of 0–3.5 cc g^{-1} , and the reported S loadings are between 50 and 80%. The large mesoporous carbons (10–50 nm) generally have higher pore volume and higher affordable S loading than microporous carbon or small mesoporous carbon. However, without further structure modification such as surface coating, the reported shuttle effect and capacity retention in DME-based electrolyte with electrodes using large mesoporous carbon were not satisfactory due to relatively weak S confinement.^[52–56]

Based on the above findings, we further explored the (de) interfacial chemistry of high Se-S loading systems using HFE-based electrolyte. Figure 7a shows the pore size distribution of two kinds of highly porous carbon (HPC). HPC1 has a main pore size of $\approx 40 \text{ nm}$, and an extremely high pore volume of 6.053 cc g^{-1} , which can theoretically load $\approx 87.5 \text{ wt\% Se-S}$. HPC2

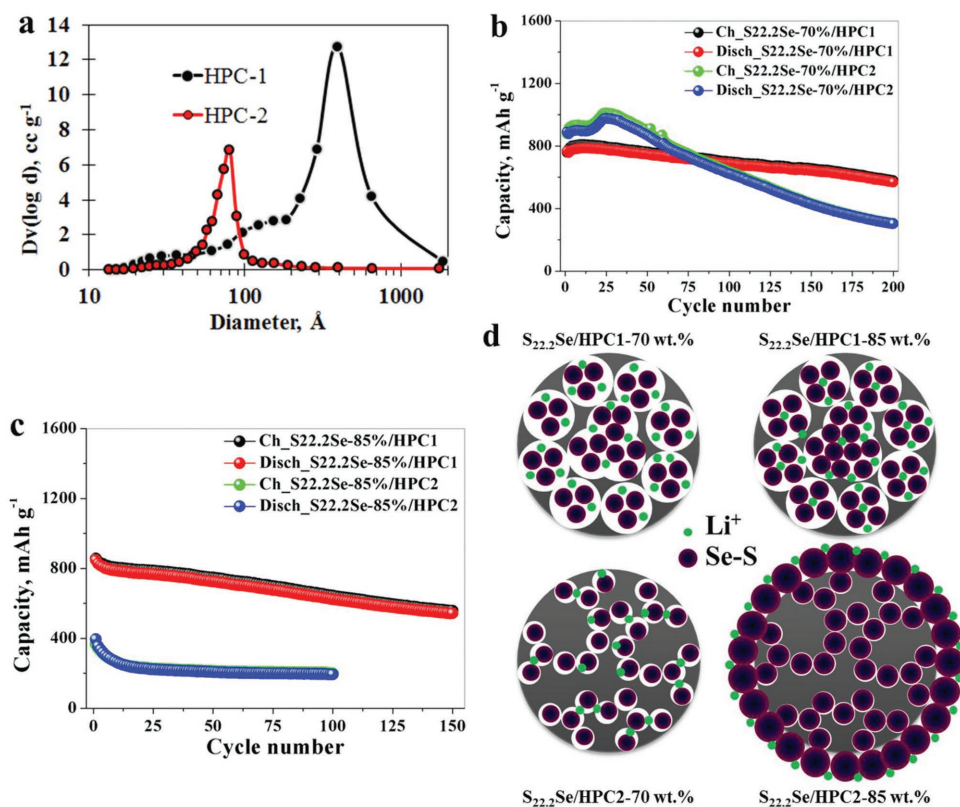


Figure 7. a) Pore size distribution of highly porous carbon with pore size of $\approx 40 \text{ nm}$ (HPC1) and 8 nm (HPC2), b) cycle performance of $S_{22.2}Se/HPC1$ (70 wt%) and $S_{22.2}Se/HPC2$ (70 wt%) at C/2 in HFE-based electrolyte, c) cycle performance of $S_{22.2}Se/HPC1$ (85 wt%) and $S_{22.2}Se/HPC2$ (85 wt%) at C/2 in HFE-based electrolyte, and d) schematic for the structures of Se-S/HPC composites.

has a smaller pore size of ≈ 8 nm and also a lower pore volume of 1.464 cc g^{-1} , which can only encapsulate 62.8 wt% Se-S in theory. We therefore prepared two Se-S/HPC composites with 70 and 85 wt% $S_{22.2}\text{Se}$ loading using HPC1 and HPC2, respectively. Figure 7b compares the cycle performance of $S_{22.2}\text{Se}/\text{HPC1}$ (70 wt%) and $S_{22.2}\text{Se}/\text{HPC2}$ (70 wt%) composites at C/2 in HFE-based electrolyte. As clearly shown, the $S_{22.2}\text{Se}/\text{HPC2}$ -70 wt% cathode can deliver relatively high initial reversible capacities of $\approx 900 \text{ mAh g}^{-1}$ at C/2. However, polysulfide/polyselenide shuttle and continuous capacity degradation were observed. After 200 cycles of charge/discharge, the reversible capacity was only 300 mAh g^{-1} . By comparison, although the reversible capacity of the $S_{22.2}\text{Se}/\text{HPC1}$ -70 wt% cathode was slightly lower ($\approx 800 \text{ mAh g}^{-1}$), the shuttle effect and the capacity retention within 200 cycles are much better than that of $S_{22.2}\text{Se}/\text{HPC2}$ -70 wt%. The capacity retention after 200 cycles at C/2 is about 74% of the first-cycle capacity, corresponding to a capacity fade rate of only $0.13\% \text{ cycle}^{-1}$. When increasing the $S_{22.2}\text{Se}$ loading to 85 wt%, as shown in Figure 7c, the $S_{22.2}\text{Se}/\text{HPC1}$ -85 wt% cathode can still deliver a reversible capacity of 542.7 mAh g^{-1} after 150 cycles with a small polysulfide/polyselenide shuttle at C/2. By contrast, the reversible capacity of the $S_{22.2}\text{Se}/\text{HPC2}$ -85 wt% cathode is only $\approx 400 \text{ mAh g}^{-1}$ and quickly faded to $\approx 200 \text{ mAh g}^{-1}$ after ten cycles, indicating very low utilization of active material. Figure S18a (Supporting Information) further shows the first three charge/discharge curves of $S_{22.2}\text{Se}/\text{HPC1}$ -85 wt% in carbonate-based electrolyte at C/10. As shown, the initial discharge capacity was only 415.2 mAh g^{-1} , while the initial charge capacity was even lower (38.5 mAh g^{-1}), which should be attributed to the accelerated nucleophilic reaction between Li_2S and carbonate-based electrolyte in the large porous carbon. The cycle performance of $S_{22.2}\text{Se}/\text{HPC1}$ -85 wt% in DME-based electrolyte is shown in Figure S18b (Supporting Information). Compared to the one in HFE-based electrolyte, $S_{22.2}\text{Se}/\text{HPC1}$ -85 wt% presents larger shuttle effect and lower reversible capacities in DME-based electrolyte. This should be owing to the weak S confinement effect of large porous carbon and the high polysulfides solubility of DME-based electrolyte. Hence, it can be clearly seen that by using HFE-based electrolyte to modify the electrode/electrolyte interface of Li/S batteries, large porous carbon that has long been regarded as inferior S host materials became effective. This finding is critical for the development of high loading Li/S batteries to increase the overall volumetric energy of batteries.

Figure 7d is a schematic for the structures of different $S_{22.2}\text{Se}/\text{HPC}$ composites. For $S_{22.2}\text{Se}/\text{HPC1}$ -70 wt% and $S_{22.2}\text{Se}/\text{HPC1}$ -85 wt%, because of the extremely high pore volume of HPC1 (6.053 cc g^{-1}), all the $S_{22.2}\text{Se}$ can be well confined within the pores, which can help to form a stable SEI layer and thus lead to good cycle stability. For $S_{22.2}\text{Se}/\text{HPC2}$ -70 wt%, all the $S_{22.2}\text{Se}$ can also be encapsulated into the mesopores of HPC2 because of its pore volume (1.464 cc g^{-1} , corresponding to maximum ≈ 75 wt% $S_{22.2}\text{Se}$ loading without considering the volume change). However, the volume change induced during charge/discharge will lead to breakup of the SEI layer and further dissociation of $S_{22.2}\text{Se}$ from the mesopores and deposit on the surface of HPC2, and thus lead to the shuttle effect and capacity fade, as observed in Figure 7b. By avoiding the effect of pore volume, we found when lowering the content of S from 70 to

60 wt%, S/HPC1-60 wt% and S/HPC2-60 wt% present similar electrochemical performance in terms of reversible capacity, coulombic efficiency, and capacity retention (Figure S19, Supporting Information), indicating pore size does not affect the electrochemical performance when all the sulfur were well confined. For $S_{22.2}\text{Se}/\text{HPC2}$ -85 wt%, all the mesopores will be filled with $S_{22.2}\text{Se}$ (75 wt%), and the excess $S_{22.2}\text{Se}$ will deposit on the surface of HPC2 and block the diffusion of Li^+ and electrons to the active material inside the pores. Therefore, very low reversible capacities were observed during charge/discharge. These results indicated that when going to high S content, pore volume may be more important to control the status of S and the associated SEI formation. In a word, it can be known that the interplay between cathode and electrolytes can significantly change the (de)lithiation chemistry and thus the electrochemical performance of space-confined Se-S cathodes.

3. Conclusion

In summary, by Se doping and rational electrode/electrolyte interface design for Li/S batteries, the sluggish electron transport and the polysulfide dissolution can be remarkably improved. This effect can be attributed to the high electronic conductivity of Se and the solid–solid lithiation chemistry enabled via a robust SEI layer. As a result, space-confined Se-S cathodes switched from the conventional two-step solid–liquid–solid reaction to solid-state (de)lithiation, as evidenced by in situ ^7Li NMR and in operando synchrotron X-ray probes. This switch directly bypassed the formation of highly soluble polysulfides/polyselenides during cycling and thus led to significantly improved electrochemical performance. Hence, Se-doped S/Ketjenblack cathode can deliver a reversible capacity of above 1000 mAh g^{-1} at C/20 within 50 cycles, 660 mAh g^{-1} at 1C after 250 cycles, and 583 mAh g^{-1} at 2C after 250 cycles, as well as an excellent rate capability of 700 mAh g^{-1} at 5C together with minimal shuttle effect. Moreover, this process also extends the optimal confinement pore size from micropores and small mesopores to large mesopores and even macropores, which can benefit the development of high-loading Li/S batteries toward high volumetric energy density. Our results indicate that manipulating the SEI interfacial chemistry via interplay between rational cathode design and optimal electrolyte could pave a new way for the development of high-performance and high-loading Li/S batteries.

4. Experimental Section

Preparation of Se-S Compounds: In a typical synthesis, sulfur powder and selenium powder were mixed in a designated weight ratio and then sealed in a glass tube under vacuum. The sealed glass tube was heated to $600 \text{ }^\circ\text{C}$ with a heating rate of $5 \text{ }^\circ\text{C min}^{-1}$ in a box furnace, and then held for 3 h before being cooled to room temperature naturally.

Preparation of Se-S/KB Composites: For the typical synthesis of $S_5\text{Se}_2/\text{KB}$ composite with a loading of 50 wt%, sulfur powder, selenium powder, and Ketjenblack (EC-600JD-AkzoNobel) were mixed at a weight ratio of 1:1:2 in a glovebox (argon filled) and then transferred to a ball milling machine and ball milled at a speed of 1425 rpm for 700 min. The weight ratio of the balls and the mixture was maintained at 10. After that, the collected powder was transferred to a sealed stainless steel

reactor and calcined at 260 °C for 24 h. The powder was collected after the temperature was cooled to room temperature. S/KB, $S_{22.2}Se/KB$, and Se/KB composites with a loading of 50 wt% were also synthesized according to the above procedure with modification on the weight ratio.

Preparation of HPC and $S_{22.2}Se/HPC$ Composite: For the synthesis of the HPC materials, a modified version of a synthesis strategy was utilized as previously employed.^[57] To summarize, a 15 wt% aqueous suspension of 4 nm colloidal silica (Alfa Aesar) was mixed under medium stirring with sucrose. For the HPC-1 sample, an amount of sucrose that maintained a 2:1 ratio (by weight) of silica to sucrose was prepared and added to the solution; for the HPC-2 sample, a 0.5:1 (by weight) ratio of silica to sucrose was used. After the components were combined into a homogeneous dispersion, the mixture was poured into an aluminum mold. The mold was placed into an open container, whereupon liquid nitrogen was poured into the container until the liquid nitrogen level was just below the top of the mold. After the mixture was completely frozen, the mold was moved into a lyophilizer (Labconco 74000 series) for freeze drying. After the water was completely removed via sublimation, the resultant material was then placed into a tube furnace (MTI GSL-1700-X), where it underwent pyrolysis under an argon environment, reaching a target temperature of 1000 °C at a ramp rate of 3 °C min⁻¹. The sample was held at 1000 °C for 3 h and afterward was cooled to room temperature at a rate of 3 °C min⁻¹. Next, the sample was placed in 3 M NaOH under medium stirring at 80 °C overnight to remove the silica, forming the mesopores. After etching the silica, the porous carbon was washed with deionized water until a pH of 7 was reached, whereupon the sample was dried in a vacuum oven at 80 °C overnight.

$S_{22.2}Se/HPC1$ and $S_{22.2}Se/HPC2$ with a $S_{22.2}Se$ loading of 70 wt% were prepared by mixing sulfur powder, selenium powder, and HPC powder in a weight ratio of 0.63:0.07:0.3 and then sealed in a glass tube under vacuum. The sealed glass tube was heated to 600 °C with a heating rate of 5 °C min⁻¹ in a box furnace, and then held for 3 h before being cooled to room temperature naturally. $S_{22.2}Se/HPC1$ and $S_{22.2}Se/HPC2$ composites with a loading of 85 wt% were also synthesized according to the above procedure with modification on the weight ratio.

Materials Characterization: The morphologies and structures of the as-prepared samples were characterized by field-emission scanning electron microscopy (HITACHI S-4700-II) and transmission electron microscopy (FEI Titan). The content of Se-S in the Se-S/C composites was measured by thermogravimetric analyses on a STA 449 F3 instrument under an argon atmosphere. High-energy synchrotron XRD measurements were carried out at Beamline 11-ID-C in Argonne National Laboratory's Advanced Photon Source (APS) using X-rays with wavelength of 0.117418 Å. The surface area, porosity, and pore size were determined in a gas sorption system (QUANTACHROME AUTOSORB 6-B). The samples were degassed at 110 °C for at least 20 h under vacuum, and then nitrogen adsorption/desorption isotherms were obtained at a constant temperature of 77.4 K. The various textural properties were all determined from the isotherms. The specific surface area was calculated by the Brunauer–Emmett–Teller (BET) method (seven points). The pore volume was estimated from single-point adsorption at a targeted relative pressure of 0.995. The pore size distribution was determined from the adsorption branch, according to the Barrett–Joyner–Halenda (BJH) method. X-ray photoelectron spectroscopy analyses were performed in ESCALAB 250Xi using a monochromatized Al K source and equipped with an Ar⁺ ion sputtering gun (Thermo Fisher). Ar⁺ etching was conducted at an argon partial pressure of 10⁻⁸ Torr in the x-y scan mode at ion acceleration of 3 kV and ion beam current density of 1 μA mm⁻².

Electrochemical Characterization: The Se-S/C laminates were prepared by spreading a mixture of 70 wt% Se-S/C composites, 20 wt% Super P, and 10 wt% sodium alginate (2.0 wt%) onto a aluminum foil current collector. The as-prepared electrodes were then dried at 60 °C in a vacuum oven for 24 h. The loading density of active materials for the Se-S/KB electrodes was controlled at about 1.5 mg cm⁻². The loading density of active materials for the Se-S/HPC electrodes was controlled at about 2.0–2.5 mg cm⁻². The electrochemical performance of the Se-S/KB

and Se-S/HPC electrodes was determined after assembling them into coin cells (type CR2032) in an argon-filled glovebox under conditions that the content of moisture and oxygen were both below 10.0 ppm. The electrode was separated from a lithium counter electrode by a separator (glass fiber, Grade GF/F Glass Microfiber Filter Binder Free, circle, 125 mm).

The electrolyte was based on DME, HFE, or carbonate. The DME-based electrolyte was composed of 1.0 M LiTFSI in DOL and DME (1/1 volume ratio) with 0.1 M LiNO₃ additive. The HFE-based electrolyte was composed of 1.0 M LiTFSI in the DOL and 1,1,2,2-tetrafluoroethyl-2,2,3,3-tetrafluoropropyl ether (1/1 volume ratio) with 0.1 M LiNO₃ additive. The carbonate-based electrolyte was composed of 1.0 M lithium hexafluorophosphate (LiPF₆) in ethylene carbonate and dimethyl carbonate (1/1 volume ratio). Also, 0.25 M Li₂S₆ catholyte was prepared by dissolving stoichiometric amounts of sulfur powder and Li₂S powder in a stoichiometric amount of DME-based electrolytes and then stirring at 50 °C overnight.

The assembled cells were charged and discharged with a MACCOR cyclor at different rates. For high-rate cycling tests (such as C/2, 1C, and 2C), the cell was subjected to three formation cycles at C/20. 1C is defined as discharge/charge the theoretical capacity of Se-S cathodes in 1 h, which is 675 mA g⁻¹ for Se, 1389 mAh g⁻¹ for S₅Se₂, and 1631 mA g⁻¹ for S_{22.2}Se, respectively.

In Situ ⁷Li NMR Cell Assembly and Measurements: A Li/S₅Se₂ pouch cell with HFE-based electrolyte was assembled in an argon-filled glovebox, and a package film (3M Scotchkap LF400M) was used to contain the cell parts and the electrolyte. The pouch cell was hermetically sealed with a heat sealer. The pouch cell was connected and tested with a portable MACCOR electrochemical test station (model 4400). In operando ⁷Li NMR measurement was carried out at 7.02 T on a Bruker Advance III WB spectrometer operating at a Larmor frequency of 116.6 MHz using a static HX probe. A $\pi/2$ pulse width of 4.25 μs was used with sufficiently long pulse recycle delay of 10 s. Chemical shifts were referenced to 1 M LiCl at 0 ppm. NMR acquisition was started simultaneously with the electrochemical cycling, and each NMR spectrum acquisition took 42 min to finish. The Li/S₅Se₂ pouch cell was cycled between 1.0 and 3.0 V at C/30 to allow enough time for NMR spectra acquisition. The data fitting of the NMR spectra was performed by using the software suite included in Bruker Topspin 3.1 to quantify the integrated areas of different species.

In Operando HEXRD and Se K-Edge XANES Measurements: Coin cells with a hole on both the top and bottom case were used for in operando X-ray experiments. In operando synchrotron HEXRD experiments were carried out at Beamline 11-ID-D of the APS using X-rays with wavelengths of 0.799898 Å. In operando XANES experiments on the Se K-edge between 12 458 and 13 458 eV were carried out in transmission mode at Beamline 20-BM-B of the APS. The incident beam was monochromatized by using a Si (111) fixed-exit, double-crystal monochromator. During the in operando experiment, a MACCOR cyclor was used to charge/discharge the cells using a constant rate of C/10 (1C = 1389 mA g⁻¹) between 1.0 and 3.0 V.

Computational Details: All the calculations, including geometry optimizations, were performed with DFT using B3LYP functional with the basis set of 6-31G(d). The SMD model in Gaussian 09 was chosen for computing the free energy (ΔG) of solvation. The computations were carried out using the program package Gaussian 09.

Supporting Information

Supporting information is available from the Wiley Online Library or from the author.

Acknowledgements

Research at the Argonne National Laboratory was funded by the U.S. Department of Energy (DOE), Vehicle Technologies Office. Use of

the Advanced Photon Source (APS) and the Center for Nanoscale Materials, both Office of Science user facilities, was supported by the U.S. Department of Energy, Office of Science, and Office of Basic Energy Sciences, under Contract No. DE-AC02-06CH11357. Support from Tien Duong of the U.S. DOE's Office of Vehicle Technologies Program is gratefully acknowledged. Sector 20 facilities at the Advanced Photon Source, and research at these facilities, were supported by DOE Basic Energy Sciences, the Canadian Light Source and its funding partners, and the APS.

Conflict of Interest

The authors declare no conflict of interest.

Keywords

(de)lithiation chemistry, cathode, electrolytes, selenium–sulfur, solid-electrolyte interphase

Received: July 19, 2018
Revised: October 29, 2018
Published online:

-
- [1] M. Armand, J. M. Tarascon, *Nature* **2008**, 451, 652.
[2] P. G. Bruce, S. A. Freunberger, L. J. Hardwick, J. M. Tarascon, *Nat. Mater.* **2012**, 11, 19.
[3] G. L. Xu, Q. Wang, J. C. Fang, Y. F. Xu, L. Huang, S. G. Sun, *J. Mater. Chem. A* **2014**, 2, 19941.
[4] W. Cai, G. Li, K. Zhang, G. Xiao, C. Wang, K. Ye, Z. Chen, Y. Zhu, Y. Qian, *Adv. Funct. Mater.* **2018**, 28, 1704865.
[5] C. P. Yang, S. Xin, Y.-X. Yin, H. Ye, J. Zhang, Y. G. Guo, *Angew. Chem., Int. Ed.* **2013**, 52, 8363.
[6] A. Abouimrane, D. Dambournet, K. W. Chapman, P. J. Chupas, W. Weng, K. Amine, *J. Am. Chem. Soc.* **2012**, 134, 4505.
[7] X. Li, J. Liang, K. Zhang, Z. Hou, W. Zhang, Y. Zhu, Y. Qian, *Energy Environ. Sci.* **2015**, 8, 3181.
[8] Y. J. Cui, A. Abouimrane, C. J. Sun, Y. Ren, K. Amine, *Chem. Commun.* **2014**, 50, 5576.
[9] B. Zhang, X. Qin, G. R. Li, X. P. Gao, *Energy Environ. Sci.* **2010**, 3, 1531.
[10] L. Hu, Y. Lu, X. Li, J. Liang, T. Huang, Y. Zhu, Y. Qian, *Small* **2017**, 13, 1603533.
[11] C. P. Yang, Y. X. Yin, Y. G. Guo, *J. Phys. Chem. Lett.* **2015**, 6, 256.
[12] G. L. Xu, J. Liu, R. Amine, Z. Chen, K. Amine, *ACS Energy Lett.* **2017**, 2, 605.
[13] S. Xin, L. Gu, N. H. Zhao, Y. X. Yin, L. J. Zhou, Y. G. Guo, L. J. Wan, *J. Am. Chem. Soc.* **2012**, 134, 18510.
[14] X. L. Ji, K. T. Lee, L. F. Nazar, *Nat. Mater.* **2009**, 8, 500.
[15] Y. Cui, A. Abouimrane, J. Lu, T. Bolin, Y. Ren, W. Weng, C. Sun, V. A. Maroni, S. M. Heald, K. Amine, *J. Am. Chem. Soc.* **2013**, 135, 8047.
[16] S. R. Chen, Y. P. Zhai, G. L. Xu, Y. X. Jiang, D. Y. Zhao, J. T. Li, L. Huang, S. G. Sun, *Electrochim. Acta* **2011**, 56, 9549.
[17] Y. X. Wang, L. Huang, L. C. Sun, S. Y. Xie, G. L. Xu, S. R. Chen, Y. F. Xu, J. T. Li, S. L. Chou, S. X. Dou, S. G. Sun, *J. Mater. Chem.* **2012**, 22, 4744.
[18] H. Sun, G. L. Xu, Y. F. Xu, S. G. Sun, X. F. Zhang, Y. C. Qiu, S. H. Yang, *Nano Res.* **2012**, 5, 726.
[19] K. Zhang, Y. Xu, Y. Lu, Y. Zhu, Y. Qian, D. Wang, J. Zhou, N. Lin, Y. Qian, *J. Mater. Chem. A* **2016**, 4, 6404.
[20] L. W. Ji, M. M. Rao, H. M. Zheng, L. Zhang, Y. C. Li, W. H. Duan, J. H. Guo, E. J. Cairns, Y. G. Zhang, *J. Am. Chem. Soc.* **2011**, 133, 18522.
[21] Q. Pang, J. T. Tang, H. Huang, X. Liang, C. Hart, K. C. Tam, L. F. Nazar, *Adv. Mater.* **2015**, 27, 6021.
[22] J. Zheng, J. Tian, D. Wu, M. Gu, W. Xu, C. Wang, F. Gao, M. H. Engelhard, J.-G. Zhang, J. Liu, J. Xiao, *Nano Lett.* **2014**, 14, 2345.
[23] Z. X. Zhao, S. Wang, R. Liang, Z. Li, Z. C. Shi, G. H. Chen, *J. Mater. Chem. A* **2014**, 2, 13509.
[24] G.-L. Xu, T. Ma, C. J. Sun, C. Luo, L. Cheng, Y. Ren, S. M. Heald, C. Wang, L. Curtiss, J. Wen, *Nano Lett.* **2016**, 16, 2663.
[25] L. Zeng, W. Zeng, Y. Jiang, X. Wei, W. Li, C. Yang, Y. Zhu, Y. Yu, *Adv. Energy Mater.* **2015**, 5, 1401377.
[26] Y. H. Qu, Z. A. Zhang, S. F. Jiang, X. W. Wang, Y. Q. Lai, Y. X. Liu, J. Li, *J. Mater. Chem. A* **2014**, 2, 12255.
[27] X. Peng, L. Wang, X. M. Zhang, B. Gao, J. J. Fu, S. Xiao, K. F. Huo, P. K. Chu, *J. Power Sources* **2015**, 288, 214.
[28] X. W. Wang, Z. A. Zhang, Y. H. Qu, G. C. Wang, Y. Q. Lai, J. Li, *J. Power Sources* **2015**, 287, 247.
[29] Z. A. Zhang, S. F. Jiang, Y. Q. Lai, J. M. Li, J. X. Song, J. Li, *J. Power Sources* **2015**, 284, 95.
[30] Z. A. Zhang, X. Yang, Z. P. Guo, Y. H. Qu, J. Li, Y. Q. Lai, *J. Power Sources* **2015**, 279, 88.
[31] C. Y. Fu, B. M. Wong, K. N. Bozhilov, J. C. Guo, *Chem. Sci.* **2016**, 7, 1224.
[32] Z. Li, L. Yuan, Z. Yi, Y. Sun, Y. Liu, Y. Jiang, Y. Shen, Y. Xin, Z. Zhang, Y. Huang, *Adv. Energy Mater.* **2014**, 4, 1301473.
[33] F. Sun, H. Cheng, J. Chen, N. Zheng, Y. Li, J. Shi, *ACS Nano* **2016**, 10, 8289.
[34] Y. S. Su, Y. Fu, T. Cochell, A. Manthiram, *Nat. Commun.* **2013**, 4, 2985.
[35] G. L. Xu, Y. F. Xu, J. C. Fang, X. X. Peng, F. Fu, L. Huang, J. T. Li, S. G. Sun, *ACS Appl. Mater. Interfaces* **2013**, 5, 10782.
[36] J. Nelson, S. Misra, Y. Yang, A. Jackson, Y. J. Liu, H. L. Wang, H. J. Dai, J. C. Andrews, Y. Cui, M. F. Toney, *J. Am. Chem. Soc.* **2012**, 134, 6337.
[37] K. A. See, M. Leskes, J. M. Griffin, S. Britto, P. D. Matthews, A. Emyl, A. Van der Ven, D. S. Wright, A. J. Morris, C. P. Grey, R. Seshadri, *J. Am. Chem. Soc.* **2014**, 136, 16368.
[38] H. Wang, N. Sa, M. He, X. Liang, L. F. Nazar, M. Balasubramanian, K. G. Gallagher, B. Key, *J. Phys. Chem. C* **2017**, 121, 6011.
[39] N. Azimi, W. Weng, C. Takoudis, Z. Zhang, *Electrochem. Commun.* **2013**, 37, 96.
[40] N. Azimi, Z. Xue, I. Bloom, M. L. Gordin, D. Wang, T. Daniel, C. Takoudis, Z. Zhang, *ACS Appl. Mater. Interfaces* **2015**, 7, 9169.
[41] T. Y. Ma, G. L. Xu, Y. Li, L. Wang, X. M. He, J. M. Zheng, J. Liu, M. H. Engelhard, P. Zapol, L. A. Curtiss, J. Jorne, K. Amine, Z. H. Chen, *J. Phys. Chem. Lett.* **2017**, 8, 1072.
[42] H. Gao, L. S. Xiao, I. Plume, G. L. Xu, Y. Ren, X. B. Zuo, Y. Z. Liu, C. Schulz, H. Wiggers, K. Amine, Z. H. Chen, *Nano Lett.* **2017**, 17, 1512.
[43] X. Q. Zeng, G. L. Xu, Y. Li, X. Y. Luo, F. Maglia, C. Bauer, S. F. Lux, O. Paschos, S. J. Kim, P. Lamp, J. Lu, K. Amine, Z. H. Chen, *ACS Appl. Mater. Interfaces* **2016**, 8, 3446.
[44] G. L. Xu, Z. Chen, G. M. Zhong, Y. Liu, Y. Yang, T. Ma, Y. Ren, X. Zuo, X. H. Wu, X. Zhang, K. Amine, *Nano Lett.* **2016**, 16, 3955.
[45] L. Suo, Y. S. Hu, H. Li, M. Armand, L. Chen, *Nat. Commun.* **2013**, 4, 1481.
[46] J. D. Thompson, C. J. Cramer, D. G. Truhlar, *J. Chem. Phys.* **2003**, 119, 1661.
[47] M. Gao, C. Su, M. He, T. Glossmann, A. Hintennach, Z. Feng, Y. Huang, Z. Zhang, *J. Mater. Chem. A* **2017**, 5, 6725.

- [48] J. Guo, X. Du, X. Zhang, F. Zhang, J. Liu, *Adv. Mater.* **2017**, *29*, 1700273.
- [49] S. S. Zhang, *J. Power Sources* **2016**, *322*, 99.
- [50] J. Liu, D. G. D. Galpaya, L. J. Yan, M. H. Sun, Z. Lin, C. Yan, C. D. Liang, S. Q. Zhang, *Energy Environ. Sci.* **2017**, *10*, 750.
- [51] S. H. Chung, C. H. Chang, A. Manthiram, *Energy Environ. Sci.* **2016**, *9*, 3188.
- [52] C. Hoffmann, S. R. Thieme, J. Brückner, M. Oschatz, T. Biemelt, G. Mondin, H. Althues, S. Kaskel, *ACS Nano* **2014**, *8*, 12130.
- [53] S. Q. Chen, B. Sun, X. Q. Xie, A. K. Mondal, X. D. Huang, G. X. Wang, *Nano Energy* **2015**, *16*, 268.
- [54] P. Strubel, S. Thieme, T. Biemelt, A. Helmer, M. Oschatz, J. Bruckner, H. Althues, S. Kaskel, *Adv. Funct. Mater.* **2015**, *25*, 287.
- [55] F. G. Sun, J. T. Wang, H. C. Chen, W. C. Li, W. M. Qiao, D. H. Long, L. C. Ling, *ACS Appl. Mater. Interfaces* **2013**, *5*, 5630.
- [56] T. Xu, J. Song, M. L. Gordin, H. Sohn, Z. Yu, S. Chen, D. Wang, *ACS Appl. Mater. Interfaces* **2013**, *5*, 11355.
- [57] L. Estevez, R. Dua, N. Bhandari, A. Ramanujapuram, P. Wang, E. P. Giannelis, *Energy Environ. Sci.* **2013**, *6*, 1785.